

## Corrosion Behavior of Mild Steel in Sour Environments at Elevated Temperatures

Shujun Gao, Peng Jin, Bruce Brown, David Young, Srdjan Nescic, Marc Singer  
Institute for Corrosion and Multiphase Technology,  
Department of Chemical & Biomolecular Engineering, Ohio University  
342 West State Street  
Athens, OH, 45701  
USA

### ABSTRACT

The objective of this work was to determine the corrosion rate of mild steel and characterize the corrosion products in sour environments at temperatures ranging from 80°C to 200°C. First, a H<sub>2</sub>S-H<sub>2</sub>O water chemistry model was developed based on available literature for a closed system at high temperature. Then, H<sub>2</sub>S corrosion tests were conducted at 80°C, 120°C, 160°C and 200°C with an exposure time of 4 days. Linear polarization resistance (LPR) and weight loss (WL) methods were used to measure the corrosion rates. X-ray diffraction (XRD) and scanning electron microscopy with energy dispersive X-ray spectroscopy microanalysis (SEM/EDS) were employed to characterize the corrosion products and surface morphology. The results show that the initial corrosion rates increased with temperature then decreased as they achieved steady-state. The corrosion product was comprised of two distinct layers. The inner corrosion product was always an iron oxide layer (hypothesized to be Fe<sub>3</sub>O<sub>4</sub>), while mackinawite, troilite, pyrrhotite and pyrite were identified as the main components of the outer layer at 80°C, 120°C, 160°C and 200°C, respectively. Pourbaix diagrams generated based on the analysis of water chemistry corroborated the experimental characterization of the corrosion products.

*Key words: hydrogen sulfide, high temperature corrosion, iron sulfide, iron oxide*

### INTRODUCTION

As geologic environments associated with oil and gas production have become increasingly aggressive, aqueous corrosion at higher temperatures in the presence of hydrogen sulfide (H<sub>2</sub>S) is more frequently encountered.<sup>Error! Reference source not found.-3</sup> High temperatures and high pressures in combination with H<sub>2</sub>S lead to many materials selection and engineering challenges, as well as potential for pipeline and equipment failures, especially in downhole environments.

H<sub>2</sub>S corrosion at low temperatures (< 80°C) has been widely studied,<sup>4-6</sup> and significant progress has been made to elucidate the general corrosion mechanisms involved. As a result, kinetic and thermodynamic models have been built and verified. It is known that the initial “bare steel” corrosion rate increases with temperature, but the increase of cathodic current is more significant than that of the anodic current.<sup>7</sup> When conditions are favorable for the formation of a corrosion product layer, its characteristics are strongly dependent on temperature. At 25°C, a porous and non-protective mackinawite layer forms on the steel surface. At 80°C, a dense and adherent corrosion product layer,

composed of mackinawite and pyrrhotite, forms that confers good protectiveness.<sup>8</sup> Temperature can accelerate both the rates of corrosion as well as the rate of corrosion product layer formation. Consequently, a peak in corrosion rate is often observed when increasing the temperature at a fixed pH<sub>2</sub>S.<sup>9</sup>

At elevated temperatures, sour corrosion has not been investigated thoroughly and the associated corrosion mechanisms are poorly understood. Until now, only a couple papers can be found on the subject in the open literature.<sup>10,11</sup> One was published more than 20 years ago and according to the authors, the corrosion rate at 220°C decreased with time due to iron sulfide growth controlled by direct reaction of H<sub>2</sub>S with the metal surface. The corrosion rate eventually reached a stable value due to the balance between layer growth and metal dissolution. Under these conditions, the major corrosion product was identified as pyrrhotite, while traces of pyrite were present. Magnetite was also identified close to the steel surface, but the authors stated that only traces could be detected.<sup>10</sup> Another more recent study identified pyrrhotite at 130°C by characterization using scanning electron microscopy (SEM) and transmission electron microscopy (TEM).<sup>11</sup>

Overall, it is expected that high temperature has a significant effect on:<sup>12-14</sup>

- Corrosion rate.
- Formation of iron sulfide polymorphs and related phases.
- Phase transformations.

Observed phases may also have interactions that lead to surface heterogeneity, onset of galvanic corrosion and localized attack.

Due to a lack of high temperature data, both the kinetic and thermodynamic models for sour environments have been verified only up to 80°C.<sup>8,15</sup> In comparison, similar models for CO<sub>2</sub> environments have already been validated for up to 250°C. It has also been reported that magnetite can form at high temperature in CO<sub>2</sub> environments and can significantly slow down the corrosion rate.<sup>16</sup> Whether or not the same is true for H<sub>2</sub>S environments is unknown.

Therefore, in order to understand, predict and mitigate H<sub>2</sub>S corrosion in oil and gas production at elevated temperatures, further experimental investigations and subsequent construction of new models of H<sub>2</sub>S corrosion are a necessity. In this work, a water chemistry model for a H<sub>2</sub>S-H<sub>2</sub>O system in a closed system at high temperatures was initially developed to better understand the water chemistry and help to properly adjust the relevant parameters in order to achieve the desired environmental conditions at a given temperature. H<sub>2</sub>S corrosion tests were then conducted at 80°C, 120°C, 160°C and 200°C, to identify the effect of high temperature on the kinetics of corrosion and layer formation on mild steel in sour environments.

## EXPERIMENTAL PROCEDURE

Experiments were performed in a 7 L Hastelloy autoclave, shown in Figure 1. A conventional three-electrode setup was used to conduct linear polarization resistance (LPR) measurements using a potentiostat. The working electrode was a cylindrical sample made from UNS K03014 (API 5L X65) carbon steel, its chemical composition shown in Table 1. A Pt-coated Nb counter electrode and a commercial Zr/ZrO<sub>2</sub> high temperature, high pressure pH probe was used as a pseudo reference electrode. The pH probe's reference serves as a reference electrode (exact potential still unknown) as long as its potential is stable at the desired test conditions.<sup>16</sup> Four flat 10×10×2 mm samples were also attached to a stabilized shaft using a PTFE-coated 304SS wire. A centrally located impeller was used to keep the solution fully mixed during each test.

The experimental conditions related to the different tested temperatures were calculated according to the water chemistry model, which will be presented later. A H<sub>2</sub>S/N<sub>2</sub> gas mixture was injected into the autoclave (no CO<sub>2</sub>); the test matrix and experimental details are summarized in Table 2 and Table 3.

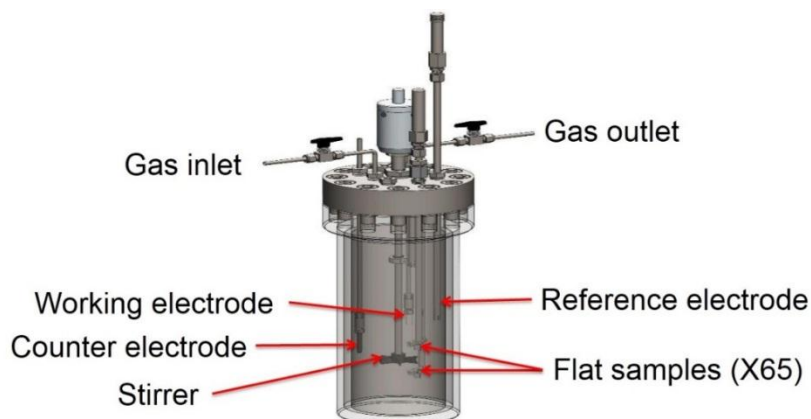


Figure 1. Experimental autoclave setup

Table 1. Chemical composition of API 5L X65 carbon steel (wt. %).

Cr	Mo	S	V	Si	C	P	Ni	Mn	Fe
0.14	0.16	0.009	0.047	0.26	0.13	0.009	0.36	1.16	Balance

Table 2. Test matrix for the effect of temperature

Parameter	Value			
Temperature, °C	80	120	160	200
pH <sub>2</sub> S, bar	0.10	0.14	0.17	0.18
Total pressure, bar	8.92	11.89	17.55	28.40
pH	4.00			
[H <sub>2</sub> S] <sub>aq</sub> , mol/L	0.00385			
Duration, days	4			

Table 3. Experimental details

Parameter	Description
System	7 L Hastelloy autoclave
Solution	1 wt.% NaCl
Specimen	API 5L X65
Stirring Speed	1000 rpm
Duration	4 days
Measurement Methods	Weight loss, LPR, EIS, (Zr/ZrO <sub>2</sub> as a pseudo reference electrode), H <sub>2</sub> S concentration (GC)
Surface Characterization	XRD, SEM/EDS, FIB-TEM, Profilometry

The following procedure was used in each test:

- The 1 wt.% NaCl solution was purged with N<sub>2</sub> overnight at room temperature;

- pH was adjusted to the calculated initial condition by using a deaerated HCl solution (1 M) (see Table 2);
- The API 5L X65 samples were mounted onto the autoclave lid and put into place;
- The electrolyte was further deoxygenated by purging with N<sub>2</sub> for another 1 hour (to avoid oxygen contamination during pH adjustment);
- The gas-out valve was closed and N<sub>2</sub> was used to pressurize the system to ensure there were no leaks;
- The system was then depressurized and H<sub>2</sub>S was rapidly introduced to the desired pressure (see Table 2);
- The autoclave was then heated up to the desired temperature in a stepwise manner to avoid overheating;
- After reaching the targeted experimental temperature, LPR was conducted between  $\pm 5$  mV vs. OCP at a scan rate of 0.125 mV/s;
- After 4 days, which was enough to get a relatively stable corrosion rate,<sup>18</sup> the autoclave was cooled to ca. 50°C;
- The H<sub>2</sub>S concentration in the gas phase was then measured by gas chromatography (GC);
- N<sub>2</sub> was used to purge the system, and remove remaining H<sub>2</sub>S, for ~3 hours;
- The autoclave lid was opened (using an H<sub>2</sub>S sensor to ensure there was no H<sub>2</sub>S remaining) and pH was measured at atmospheric conditions; then the Fe<sup>2+</sup> concentration of the solution determined using a spectrophotometer;
- The corroded samples were retrieved and characterized by X-ray diffraction (XRD), scanning electron microscopy/energy dispersive X-ray spectroscopy (SEM/EDS), and surface profilometry.

## RESULTS

The presentation of the results is divided in two main parts: water chemistry model development and experimental corrosion study at elevated temperature.

### Water Chemistry at High Temperatures in a Closed System

#### Model Construction

In order to define the experimental parameters such as pressure of H<sub>2</sub>S and pH in the autoclave, a water chemistry model at high temperatures for a closed (constant inventory) system was developed. The experimental autoclave was identified as a closed system since it was closed after initially purging with gas to a designated pressure. Unlike an open system (typically a purged glass cell), the gas partial pressures in a closed system are not constant; e.g. the H<sub>2</sub>S in the gas phase dissolves in water to a given extent depending on temperature and pH, and is not replenished. It is actually extremely difficult to adjust parameters such as solution pH once the system has been pressurized. Instead, a different approach was taken which involves the accurate determination for the corresponding conditions (pH, and p<sub>H<sub>2</sub>S</sub>) at ambient temperature and atmospheric conditions, which will lead to the desired conditions once the autoclave is closed and the elevated temperature is reached. The process is shown in Figure 2 and presented described as follows:

- Input the desired parameters of T, p<sub>H<sub>2</sub>S</sub> and pH at equilibrium for the operating conditions (high temperature);
- Set the volume ratio between liquid phase and gas phase inside the autoclave;
- Use a molar balance for sulfur species in the autoclave; calculate the dissolution and dissociation constants;
- Considering a closed system, calculate the corresponding parameters at 25°C and use them as the initial set of conditions.

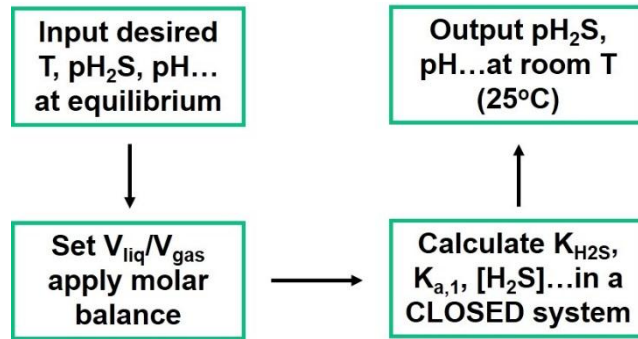


Figure 2. Process of modeling the water chemistry in a closed system at high temperatures.

Care must be taken to select the correct expressions for physical properties and equilibrium constants that are valid at high temperatures. The first important property is the water density, since it experiences considerable changes at high temperatures and will significantly affect the water chemistry. The most widely accepted expression was reported by Jones and Harris:<sup>19</sup>

$$\rho = \frac{999.83952 + T_c(16.945176 + T_c(-7.9870401 \times 10^{-3} + T_c(-46.170461 \times 10^{-6} + T_c(105.56302 \times 10^{-9} - 280.54253 \times 10^{-12} T_c))))}{1.0 + 16.87985 \times 10^{-3} T_c} \quad (1)$$

where  $\rho$  is water density in kg/m<sup>3</sup>, and  $T_c$  is temperature (in °C). This expression was selected to be used in this model because of its widespread adoption, e.g, in the International Temperature Scale (ITS).

The the equilibrium constants  $K_{H_2S}$ ,  $K_{a,1}$  and  $K_{a,2}$  calculated based on the research described by Suleimenov<sup>20,21</sup> and Ning<sup>22</sup> (Equations (2)-(10)), but modified from molality to molarity units. Originally, these values were as molality units (mol/kg bar), but were here used in molarity (mol/L bar) since the numerical values are very close at temperatures under 100°C.<sup>7,22</sup> However, as shown in Figure 3, when used at higher temperature (typically above 100°C), large differences can appear (for example, more than 25% error is apparent at 250°C).



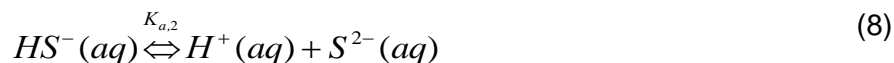
$$K_{H_2S} = \frac{[H_2S]}{P_{H_2S}} \quad (3)$$

$$K_{H_2S} = 10^{-(634.27 + 0.2709T_K - 0.0001113T_K^2 - 16719T_K - 2619 \log T_K)} \quad (4)$$



$$K_{a,1} = \frac{[H^+][HS^-]}{[H_2S]} \quad (6)$$

$$K_{a,1} = 10^{782.439450.36126T_K - 1.6722 \times 10^{-4} T_K^2 - 20565.7315T_K - 142.741722 \ln T_K} \quad (7)$$



$$K_{a,2} = \frac{[H^{+}][S^{2-}]}{[HS^{-}]} \quad (9)$$

$$K_{a,2} = 10^{-(23.93-0.030446T+2.483 \times 10^{-5}T_K^2)} \quad (10)$$

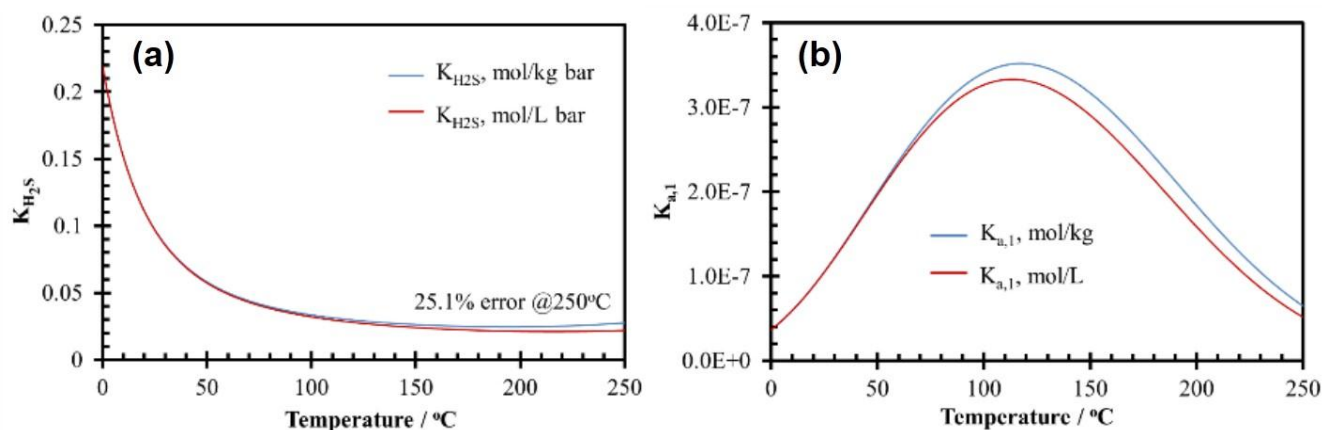


Figure 3. (a)  $K_{H_2S}$  and (b)  $K_{a,1}$  values with respect to molality and molarity at different temperatures.

### Parametric Study

A parametric study was completed to predict the calculated variation of species concentrations at different temperatures. This was an essential step in properly designing any experimental conditions. The effect of  $V_{liq}/V_{gas}$  ratio on the water chemistry is shown in Figure 4. Being able to anticipate and understand the effect of this ratio is important since, ideally, the test conditions should simulate an open system where the partial pressure of  $H_2S$  is constant. This is not possible in an autoclave setup but the characteristics of an open system can be closely approached if the right conditions are selected. Figure 4 shows that the behaviors of  $[H_2S]_{aq}$ ,  $[HS^{-}]$ , and  $[S^{2-}]$  concentrations are different in an open and closed system at higher pH values. The discrepancy is more apparent at a higher liquid/gas volume ratio (*i.e.*, a large volume of liquid). The total amount of  $H_2S$  (sum of all the sulfide species) that needs to be injected into the 7 L autoclave increases with decreasing gas volume for a fixed  $H_2S$  partial pressure and pH 4.00. On the other hand, choosing a low liquid volume would lead to rapid change in chemistry due to the generation of corrosion products. At a  $V_{liq}/V_{gas}$  ratio of 6, the discrepancy between open and closed systems is minimized. This ratio is therefore chosen in this work for every experimental temperature.

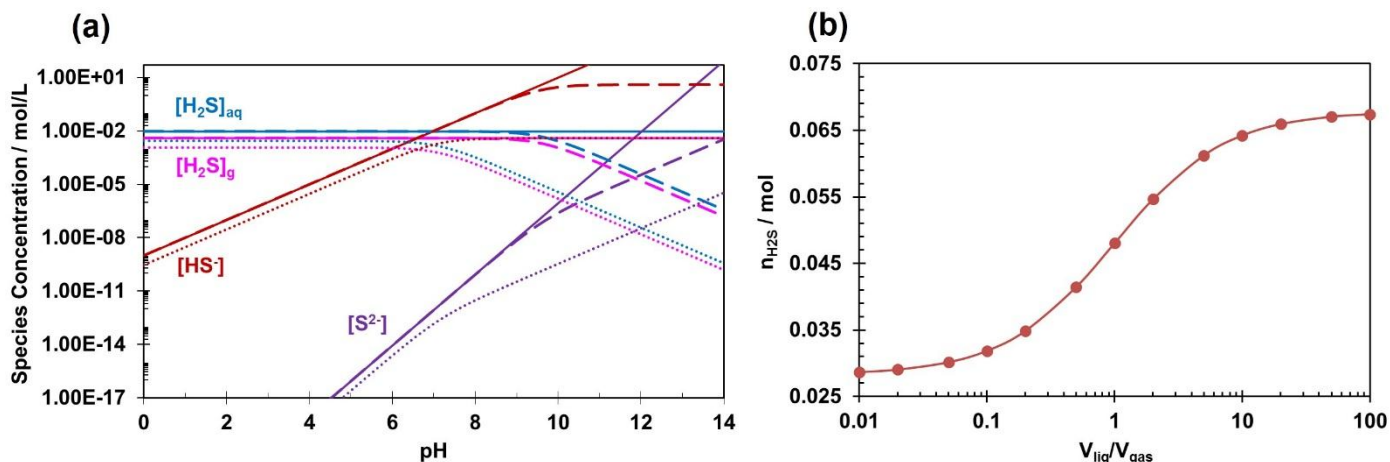


Figure 4. (a) Effect of  $V_{liq}/V_{gas}$  ratio on the concentrations of sulfur species, and (b) the total amount of  $H_2S$  in a 7 L autoclave at pH 4.00,  $T=25^\circ C$ ,  $p_{H_2S}=0.10$  bar.

The effect of temperature on the concentrations of sulfide species at a fixed pH 4.00 and 0.10 bar pressure of  $H_2S$  is shown in Figure 5(a). All the species concentrations significantly vary with increasing temperature. However, what really matters for corrosion is not  $p_{H_2S}$ , but the concentration of dissolved  $H_2S$  in the solution,  $[H_2S]_{aq}$ . In this work,  $[H_2S]_{aq}$  was kept at 0.00385 mol/L for every temperature to enable better comparisons. This corresponds to 0.10 bar  $H_2S$  at  $80^\circ C$ . In order to maintain  $[H_2S]_{aq}$  as a constant at higher temperatures, the  $p_{H_2S}$  needs to be increased (Figure 5(b)).  $H_2S$  corrosion at  $80^\circ C$ ,  $120^\circ C$ ,  $160^\circ C$ , and  $200^\circ C$  at a constant  $[H_2S]_{aq}$  will be investigated in this work.

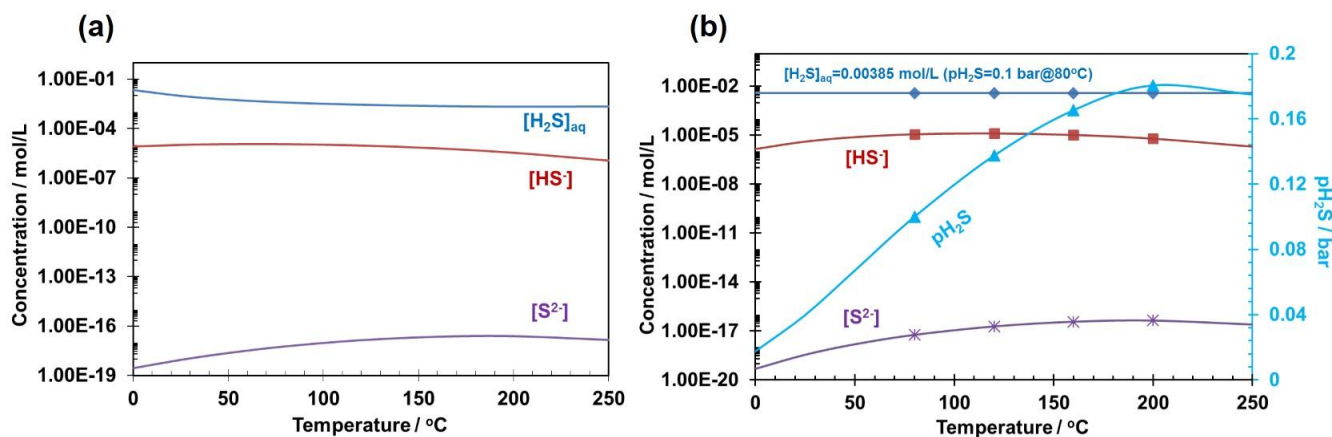


Figure 5. Effect of temperature on concentrations of sulfur species at (a) constant  $p_{H_2S}=0.10$  bar and (b) constant  $[H_2S]_{aq}=0.00385$  mol/L ( $p_{H_2S}=0.10$  bar@ $80^\circ C$ ), pH=4.00.

Experimentally, the water chemistry at high temperature should be monitored and compared with theoretical values. However, due to the lack of a reliable reference electrode in high temperature and high pressure  $H_2S$  environments, pH could not be measured *in situ*. Therefore, the water chemistry verification could not be directly done, but had to be back-calculated by characterization of liquid samples taken at the end of each experiment.

### Effect of High Temperature on $H_2S$ Corrosion

Experiments based on the test matrix in Table 2 were performed to identify the effect of high temperature on the kinetics of corrosion and layer formation on mild steel in sour environments. The results are presented below.

## Corrosion Rates

Figure 6 shows the corrosion rates over time at 80°C, 120°C, 160°C, and 200°C as measured by LPR. It can be seen that the initial corrosion rates increased with increasing temperature, and then quickly decreased to stable corrosion rates of 4.1, 3.8, 1.8 and 2.5 mm/y, respectively, from lowest to highest temperature. Overall, the steady-state corrosion rate decreased with temperature except at 200°C.

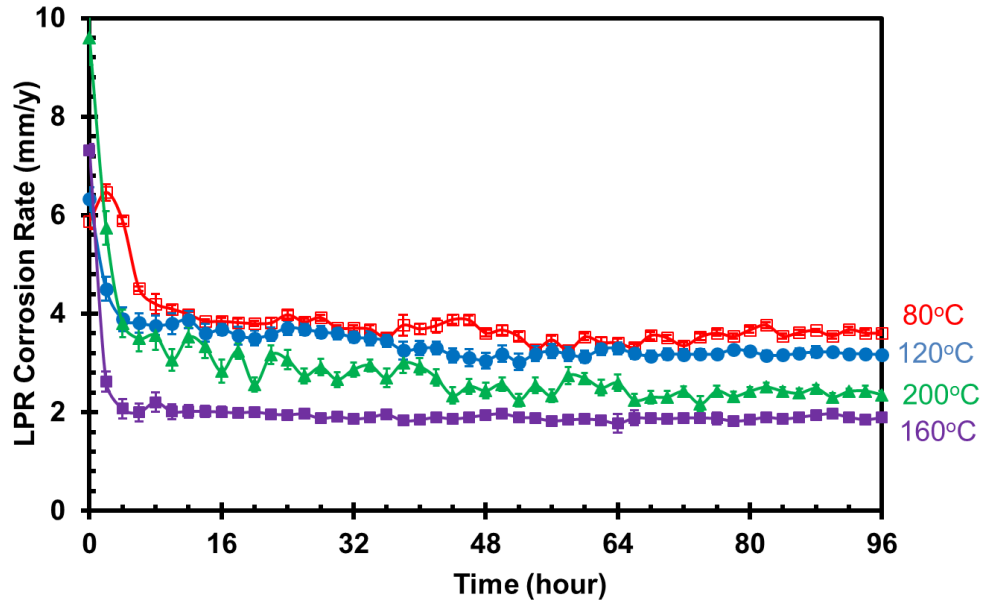


Figure 6. Corrosion rate at different temperatures from LPR measurement,  $[H_2S]_{aq}=0.00385$  mol/L, pH=4.00, 4 days, B=23 mV/decade.

The time-averaged corrosion rates obtained from weight loss are shown in Figure 7. They are in good agreement with the time-integrated corrosion rate from LPR using a B value of 23 mV/decade.

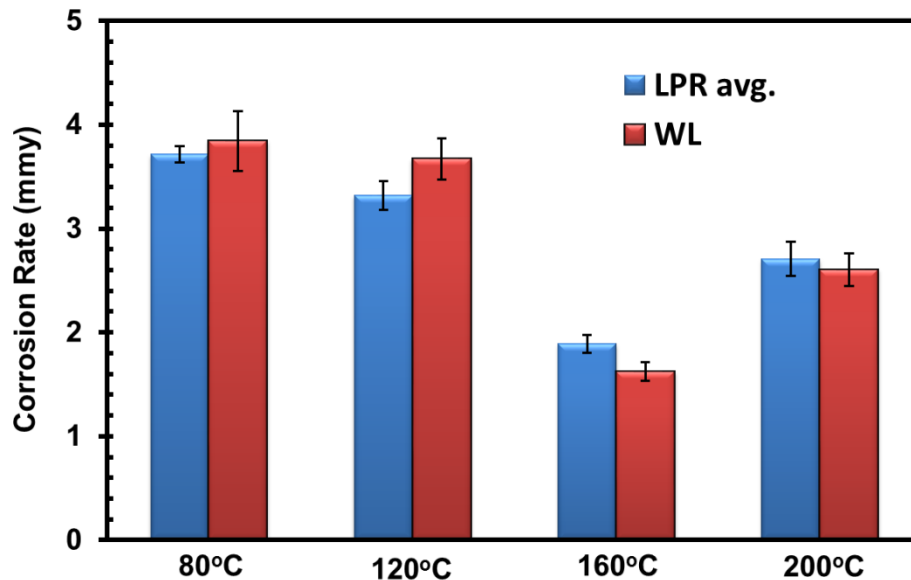


Figure 7. Comparison of corrosion rates between LPR and weight loss,  $[H_2S]_{aq}=0.00385$  mol/L, pH=4.00, 4 days, B=23 mV/decade.

## Corrosion Products

The corrosion products on the steel surface were characterized by XRD as shown in Figure 8. While mackinawite (FeS) was the main corrosion product detected at 80°C, troilite (FeS), pyrrhotite (Fe<sub>1-x</sub>S, x=0~0.17) and pyrrhotite/pyrite (FeS<sub>2</sub>) became the dominant species as temperature was increased. With increasing temperature, the corrosion product became richer in sulfur; this is an indication of enhanced reaction kinetics for phase transformations.

The morphologies of the formed corrosion products were also characterized by SEM, as shown in Figure 9 and Figure 10. The SEM for the 80°C specimen shows a mackinawite layer of 15 µm thickness, which is much thinner than the corresponding metal loss thickness calculated to be 42 µm. From the EDS line scan, the outer layer was identified to be likely an iron sulfide but an inner layer, which consisted mostly of iron and oxygen was probably an iron oxide. At 120°C, the SEM shows troilite-like crystals on the surface and a much thicker layer (61~73 µm). The α-Fe peaks are absent in the XRD pattern as the corrosion product is so thick, preventing the X-rays from reaching the metal substrate. At 160°C, pyrrhotite crystals were clearly observed. The thickness of the layer was only about 10 µm, but still no α-Fe peaks were detected by XRD, indicating the corrosion product layer was very dense and compact. This is also probably why the corrosion rate at 160°C was the lowest. The corrosion products changed to planar flaky crystals at 200°C. All the cross-sections show a two-layer structure at every temperature tested: an inner layer comprised of an iron oxide and an outer layer comprised of an iron sulfide. However, the iron oxide was not detected by XRD due to the top layer being too thick and compact for XRD penetration.

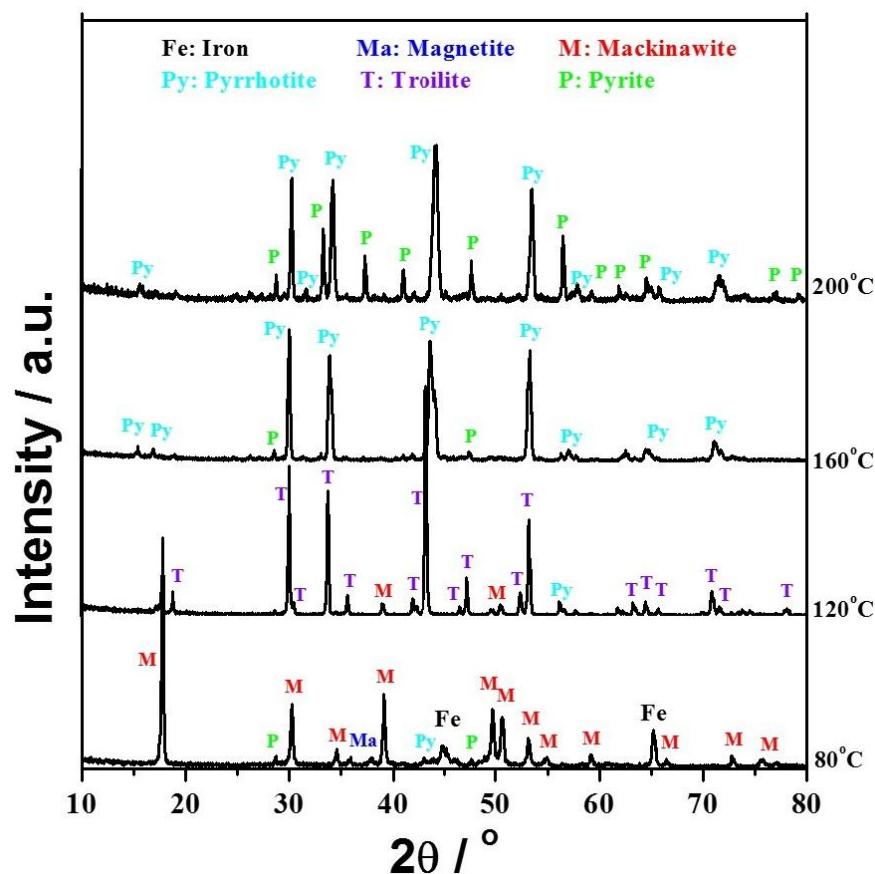


Figure 8. XRD patterns of corrosion products on the steel surface at different temperatures, [H<sub>2</sub>S]<sub>aq</sub>=0.00385 mol/L, pH=4.00, 4 days.

©2017 by NACE International.

Requests for permission to publish this manuscript in any form, in part or in whole, must be in writing to NACE International, Publications Division, 15835 Park Ten Place, Houston, Texas 77084.

The material presented and the views expressed in this paper are solely those of the author(s) and are not necessarily endorsed by the Association.

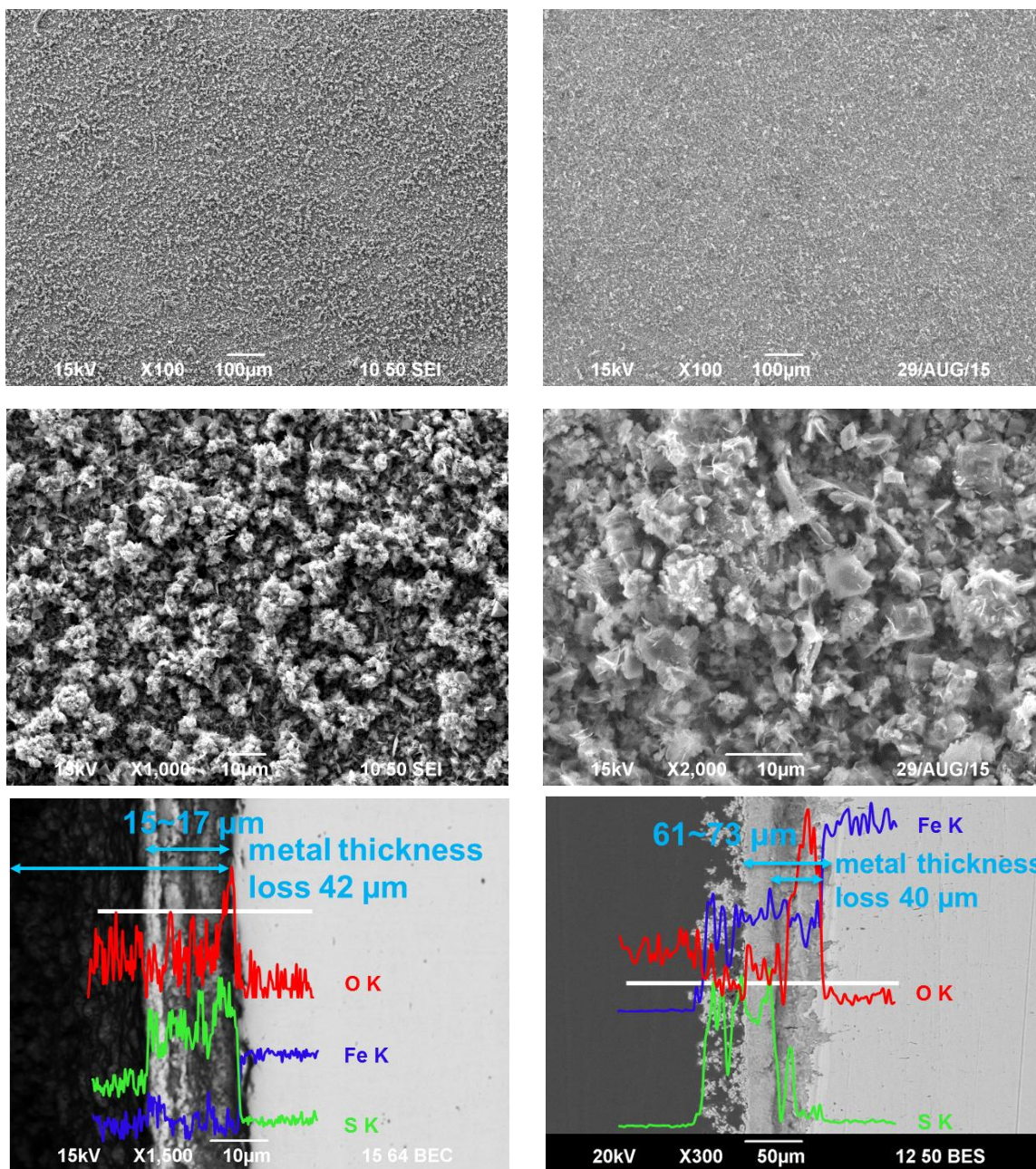


Figure 9. SEM of morphologies and cross-sections at 80°C (left) and 120°C (right),  $[H_2S]_{aq}=0.00385$  mol/L, pH=4.00, 4 days.

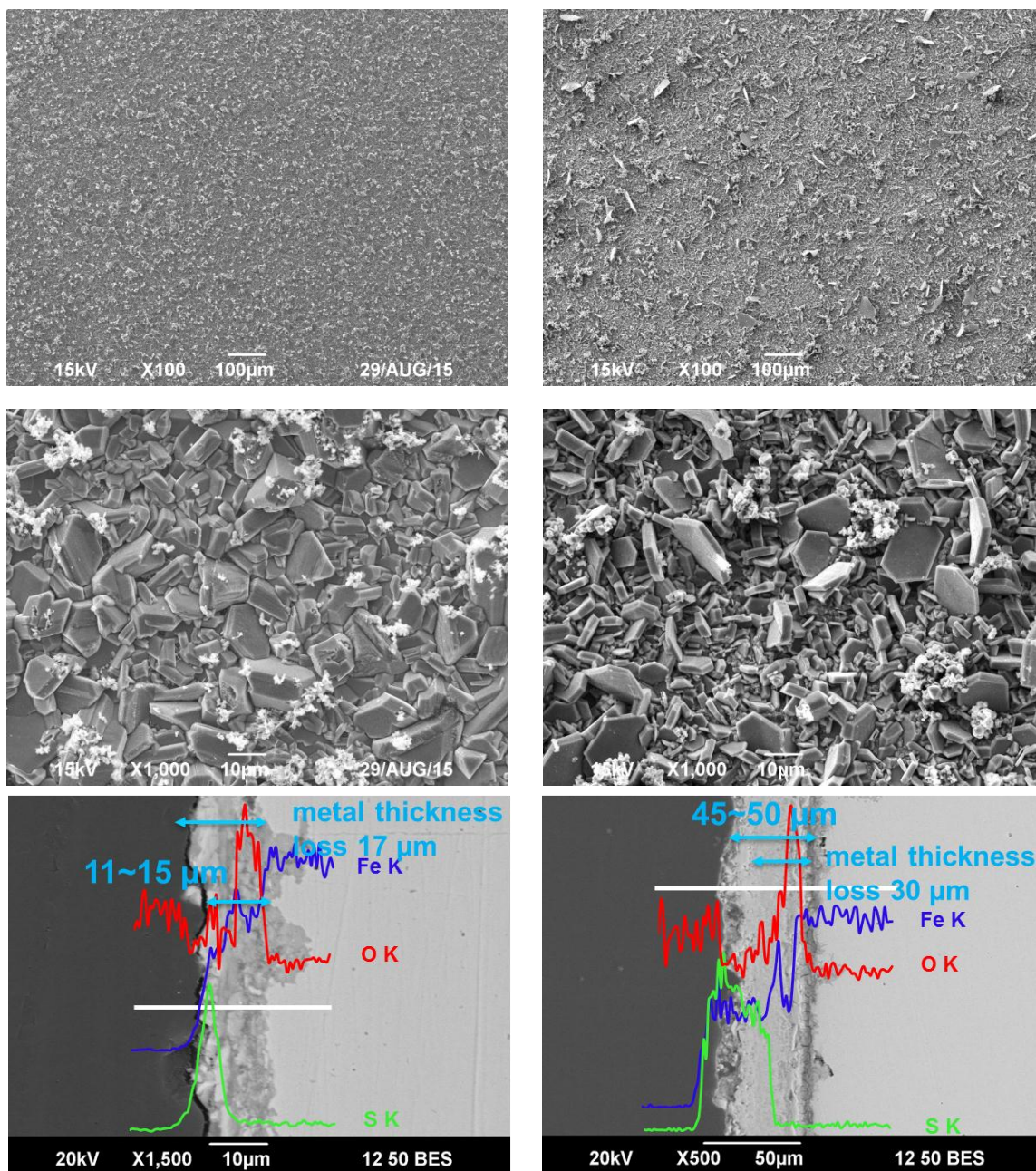


Figure 10. SEM of morphologies and cross-sections at 160°C (left) and 200°C (right),  $[H_2S]_{aq}=0.00385$  mol/L, pH=4.00, 4 days.

### Surface Profilometry

After removal of the corrosion products using Clarke solution,<sup>23</sup> the metal surface was characterized by profilometry, as shown in Figure 11 and Figure 12. No obvious localized corrosion was observed at 80°C and 120°C. The surface was relatively smooth and the corrosion could be considered as uniform. However, at 160°C some small pits could be observed with around a 1.2 pitting ratio (ratio of maximum pit rate to general corrosion rate) and 1.5 mm/y pit penetration rate. This can be treated only as localized corrosion initiation. At 200°C, many large pits appeared with a 3.2 pitting ratio and 8.2 mm/y pit penetration rate. The pitting ratio is not accurate since the pitting corrosion overwhelmed the whole general corrosion. Due to severe localized corrosion at this temperature, the stable LPR corrosion rate

©2017 by NACE International.

Requests for permission to publish this manuscript in any form, in part or in whole, must be in writing to NACE International, Publications Division, 15835 Park Ten Place, Houston, Texas 77084.

The material presented and the views expressed in this paper are solely those of the author(s) and are not necessarily endorsed by the Association.

was a little higher than at 160°C (Figure 6). These results fit with Ning's previous work<sup>24</sup> where it was found that once there is pyrite formation, localized attack would occur.

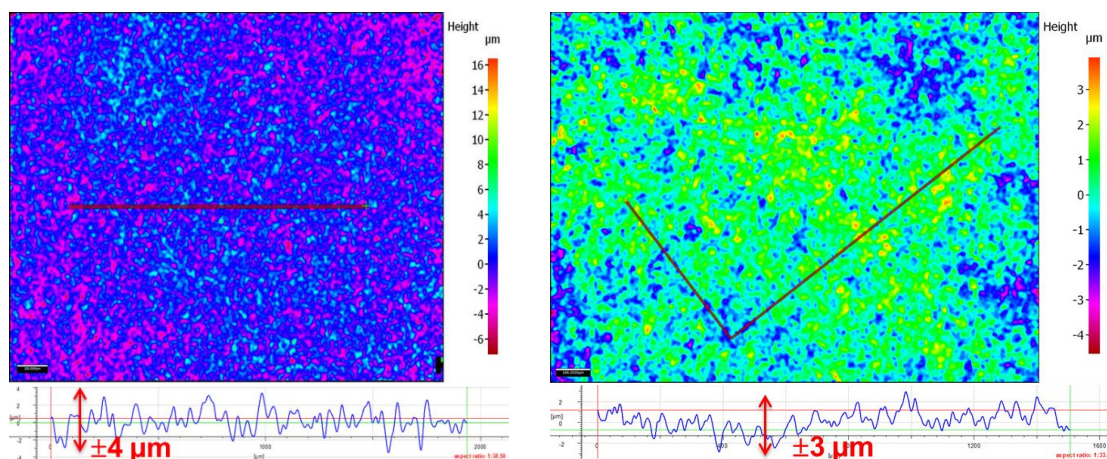


Figure 11. Surface profilometry after removing corrosion products at 80°C (left) and 120°C (right),  $[H_2S]_{aq}=0.00385$  mol/L, pH=4.00, 4 days.

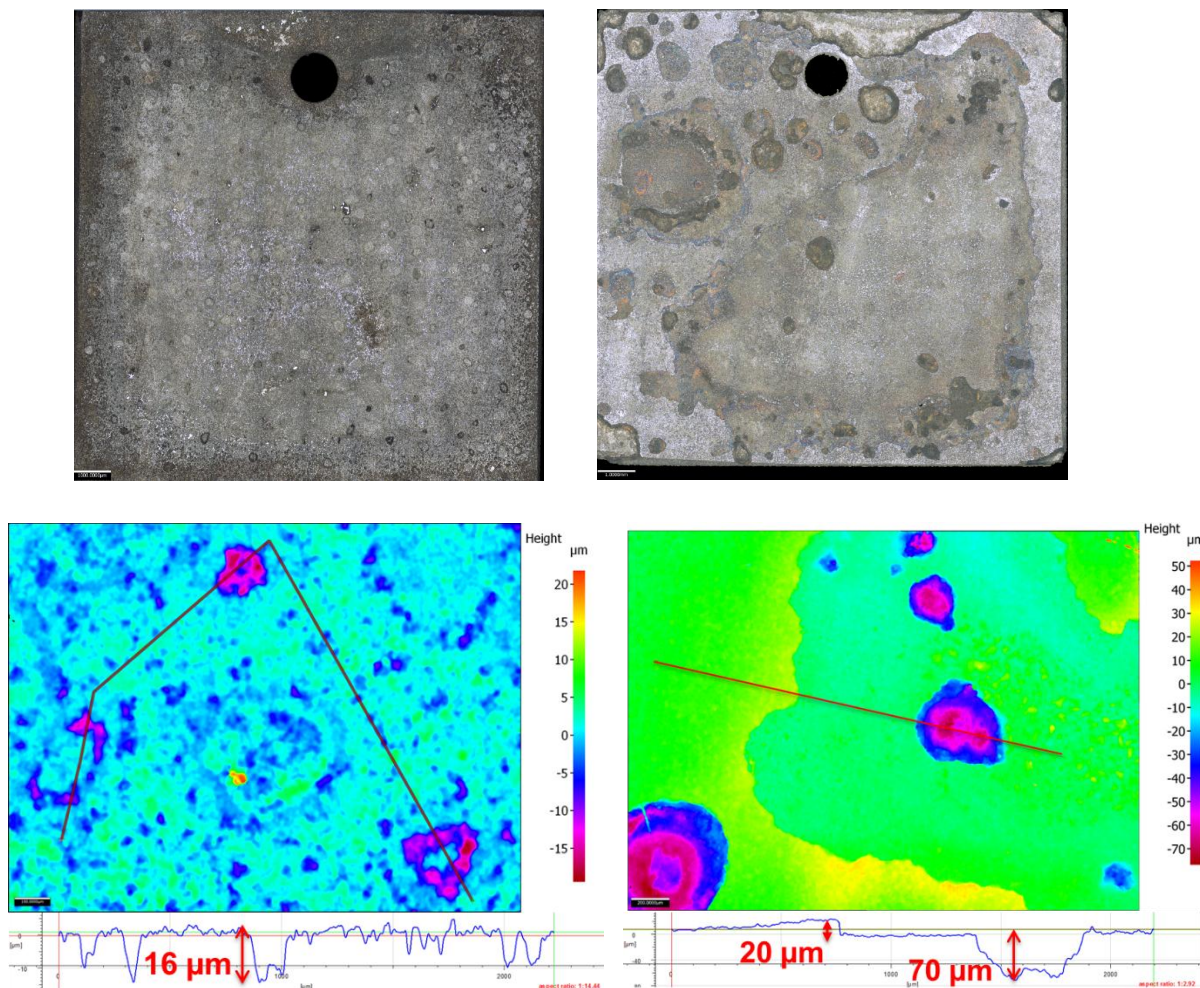


Figure 12. Surface profilometry after removing corrosion products at 160°C (left) and 200°C (right),  $[H_2S]_{aq}=0.00385$  mol/L, pH=4.00, 4 days.

## DISCUSSION

The current results are insufficient to make conclusive mechanistic statements, however, there are some new findings that are worthy of a discussion, especially in the context of the existing literature.

### Formation of Iron Oxide

Iron oxide was found, at every temperature tested, as the main component of the inner corrosion product layer (Figure 9 and Figure 10). Until now, iron oxide has not been given much attention as a corrosion product in H<sub>2</sub>S corrosion environments. It is hypothesized that this iron oxide is magnetite (Fe<sub>3</sub>O<sub>4</sub>) due to the following observations:

- Two Fe<sub>3</sub>O<sub>4</sub> peaks were observed from XRD analysis at 80°C (Figure 8), though they were not detected at other temperatures due to the top layer being either too thick or too compact for X-ray penetration;
- Fe<sub>3</sub>O<sub>4</sub> was also confirmed as an inner layer from a previous study in sour environments at 220°C;<sup>10</sup>
- Fe<sub>3</sub>O<sub>4</sub> is also the main corrosion product at high temperatures in CO<sub>2</sub> environments.<sup>16</sup>

The kinetics of Fe<sub>3</sub>O<sub>4</sub> formation is very fast, making the scaling tendency (ST that is the ratio of precipitation rate to corrosion rate) very high at high temperature. Fe<sub>3</sub>O<sub>4</sub> can form on the metal surface according to reaction (11):



From the Pourbaix diagram shown in Figure 13, considering a sweet (CO<sub>2</sub> dominated) system, Fe<sub>3</sub>O<sub>4</sub> is dominant in a very limited narrow area at potentials more positive than those for FeCO<sub>3</sub> at 80°C. When the temperature increases to 200°C, the possibility for Fe<sub>3</sub>O<sub>4</sub> of being the dominant species is greatly increased. Similarly, in sour corrosion at high temperature, the iron oxides should be taken into account, along with the iron sulfides.

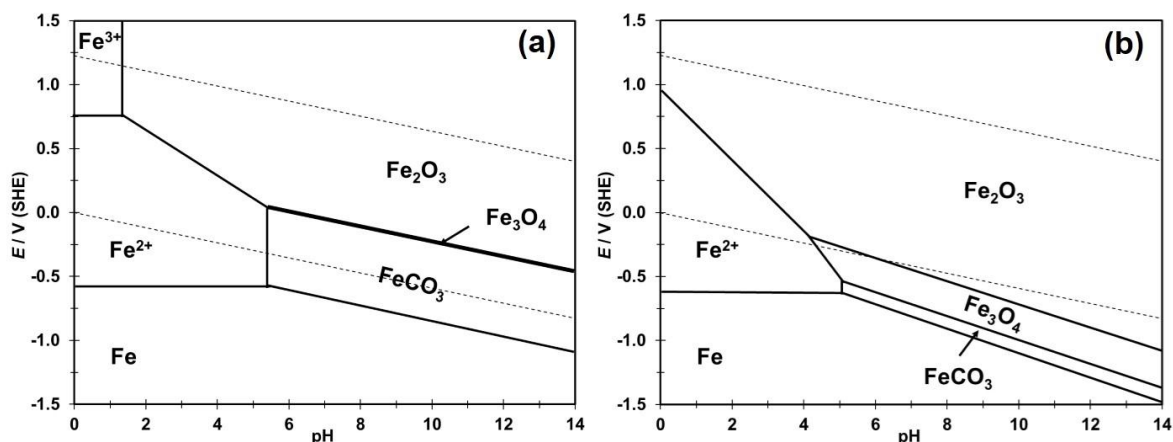


Figure 13. Pourbaix diagram for Fe-CO<sub>2</sub>-H<sub>2</sub>O system (a) at 80°C and (b) 200°C, 1 bar CO<sub>2</sub> at 25°C.

### Formation of Iron Sulfide

The objective of this section is to compare the thermodynamic predictions for the formation of corrosion products with the experimental results. The thermodynamic prediction model is based on Ning's work,<sup>8</sup>

©2017 by NACE International.

Requests for permission to publish this manuscript in any form, in part or in whole, must be in writing to

NACE International, Publications Division, 15835 Park Ten Place, Houston, Texas 77084.

The material presented and the views expressed in this paper are solely those of the author(s) and are not necessarily endorsed by the Association.

which has not been verified above 80°C. In order to do so, a good understanding of the water chemistry at operating conditions needed to be developed. Since no direct measurement of pH and Fe<sup>2+</sup> concentration could be performed *in situ*, some assumptions are needed as described below.

The H<sub>2</sub>S concentration and Fe<sup>2+</sup> concentration were measured using GC and spectrophotometry, respectively, after cooling down the autoclave (usually to around 50°C). The water chemistry was calculated at this measured temperature according to Equations (3), (6), (9), (13), and (15):



$$K_w = [H^+][OH^-] \quad (13)$$

$$K_w = 10^{-(29.3868 - 0.073754T_K + 7.4788 \times 10^{-5} T_K^2)} \quad (14)$$

$$[Na^+] + 2[Fe^{2+}] + [H^+] = [Cl^-] + [HS^-] + 2[S^{2-}] + [OH^-] \quad (15)$$

In Equation (15), for determining electroneutrality, the [Cl<sup>-</sup>] is known experimentally by recording how much NaCl and HCl (for pH adjustment) were added. There are 5 equations and 5 unknowns ([H<sub>2</sub>S], [HS<sup>-</sup>], [S<sup>2-</sup>], [H<sup>+</sup>], and [OH<sup>-</sup>]). The total amount of sulfur species was calculated by applying a molar balance:

$$\sum S = [H_2S]_g + [H_2S]_{aq} + [HS^-]_{aq} + [S^{2-}]_{aq} = constant \quad (16)$$

It is assumed that no significant gain or loss of Fe<sup>2+</sup> occurred during the test “cooling down” procedure, either by FeS precipitation or dissolution. The [Fe<sup>2+</sup>] concentration measured at the sampling temperature was assumed to be the same as under operating conditions. At the experimental temperature pH<sub>2</sub>S is also unknown, in addition to the 5 unknowns mentioned above, but the extra equation (16) can be used. The calculation results are summarized in Table 4.

Table 4. Summary of initial conditions and theoretical calculated final conditions.

T, °C	Initial Conditions		Final Conditions		
	pH <sub>2</sub> S, bar	pH	pH <sub>2</sub> S, bar	pH	Fe <sup>2+</sup> , ppm
80	0.10	4.00	0.07	5.47	1.79
120	0.14	4.00	0.11	5.42	5.82
160	0.14	4.00	0.14	5.48	4.26
200	0.18	4.00	0.16	5.78	2.31

Compared with the initial conditions, the final pH values all drifted from 4.00 to above 5.40, which represent conditions increasingly favorable for iron sulfide formation. These parameters are used to generate Pourbaix diagrams as shown in Figure 14. The red arrow represents the pH shifting and the likely potential range (around -500 mV vs. SHE).

The Pourbaix diagrams provide useful information to understand the experimental results. Different polymorphs and related phases of iron sulfides were identified at the different temperatures tested. Fe<sub>3</sub>O<sub>4</sub> and mackinawite were always observed after short exposure times, inferring that they always formed first. However, according to the Pourbaix diagrams in H<sub>2</sub>S environments, pyrite and pyrrhotite should be more stable than iron oxides and mackinawite, which act as precursors for the transformation reactions.<sup>25</sup> However, pyrrhotite and pyrite were only observed at 160°C and 200°C. This could be explained considering that the transformation kinetics are accelerated at higher temperatures. Particularly at 200°C, the “pH shift” arrow crosses the equilibrium line between pyrrhotite and pyrite,

indicating a possible iron sulfide transformation between pyrrhotite and pyrite, which is in good agreement with the XRD data (Figure 8).

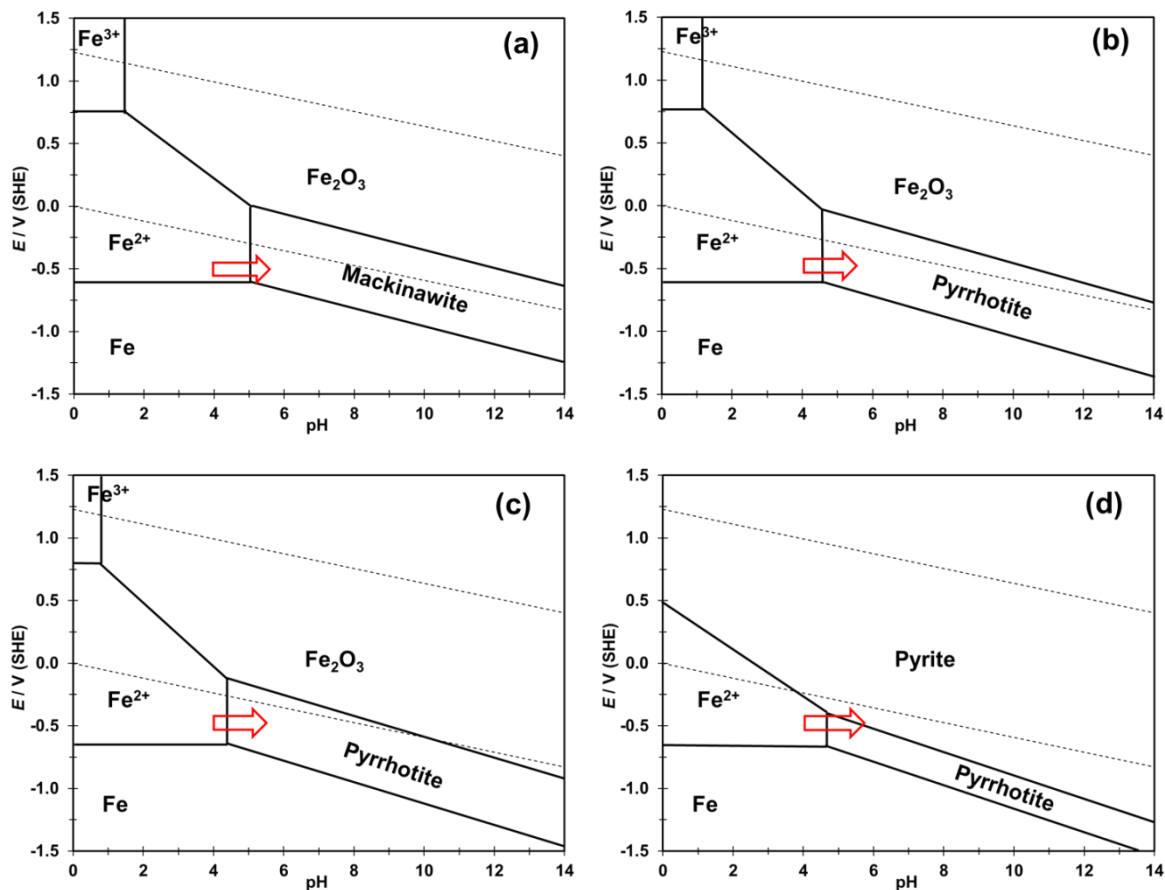


Figure 14. Pourbaix diagram for Fe-H<sub>2</sub>S-H<sub>2</sub>O system, (a) 80°C, mackinawite, (b) 120°C, pyrrhotite (troilite), (c) 160°C, pyrrhotite, and (d) 200°C, pyrite/pyrrhotite, other input parameters are in Table 4.

## CONCLUSIONS

- A water chemistry model for a closed system containing H<sub>2</sub>S was developed and checked for validity at high temperatures.
- Sour corrosion experiments were conducted successfully at 80°C, 120°C, 160°C and 200°C. Initial corrosion rates increased with increasing temperature. Final corrosion rates, after 4 days of exposure, remained high at between 2 and 4 mm/y.
- Iron sulfide transformation was observed for the first time in high temperature H<sub>2</sub>S corrosion. The inner corrosion product was iron oxide (postulated to be Fe<sub>3</sub>O<sub>4</sub>), the outer layer was mainly mackinawite, troilite, pyrrhotite and pyrite at 80°C, 120°C, 160°C and 200°C, respectively.

## ACKNOWLEDGEMENTS

The authors would like to express sincere appreciation to the following industrial sponsors for their financial support and direction: Anadarko, Baker Hughes, BP, Chevron, China National Offshore Oil Corporation, ConocoPhillips, DNV GL, ExxonMobil, M-I SWACO, Occidental Oil Company, Petroleum Institute, PTT, Saudi Aramco, Shell Global Solutions, SINOPEC, TOTAL, TransCanada, WGK.

## REFERENCES

1. G. DeBruijn, "High-pressure, high-temperature technologies," *Oilfield Review* 20, 3(2008): p. 46-60.
2. H.J. Chen, "High temperature corrosion inhibition performance of imidazoline and amide," CORROSION/2010, paper no. 00035 (San Antonio, TX: NACE, 2010).
3. S.S. Prabha, "Corrosion problems in petroleum industry," *European Chemical Bulletin* 3, 3 (2014): p. 300-307.
4. H. Ma, X. Cheng, G. Li, S. Chen, Z. Quan, S. Zhao, L. Niu, "The influence of hydrogen sulfide on corrosion of iron under different conditions," *Corrosion Science* 42, 10 (2000): p. 1669-1683.
5. W. Sun, S. Nescic, S. Papavinasam, "Kinetics of iron sulfide and mixed iron sulfide/carbonate scale precipitation in CO<sub>2</sub>/H<sub>2</sub>S corrosion," CORROSION/2006, paper no. 06644 (San Diego, CA: NACE, 2006).
6. J. Tang, Y. Shao, J. Guo, T. Zhang, G. Meng, F. Wang, "The effect of H<sub>2</sub>S concentration on the corrosion behavior of carbon steel at 90°C." *Corrosion Science* 52, 6 (2010): p. 2050-2058.
7. Y. Zheng, B. Brown, S. Nescic, "Electrochemical study and modeling of H<sub>2</sub>S corrosion of mild steel," *Corrosion*, 70, 4 (2013): p. 351-365.
8. J. Ning, Y. Zheng, B. Brown, D. Young, and S. Nescic, "A Thermodynamic Model for the Prediction of Mild Steel Corrosion Products in an Aqueous Hydrogen Sulfide Environment," *Corrosion*, 71, 8 (2015): p. 945-960.
9. W. Sun, D.V. Pugh, S.N. Smith, S. Ling, J.L. Pacheco, R.J. Franco, "A parametric study of sour corrosion of carbon steel," CORROSION/2010, paper no. 10278 (San Antonio, TX: NACE, 2010).
10. T.A. Ramanarayanan, S.N. Smith, "Corrosion of Iron in Gaseous Environments and in Gas-Saturated Aqueous Environments," *Corrosion*, 46, 1 (1990): p. 66-74.
11. F. Shi, L. Zhang, J. Yang, M. Lu, J. Ding, H. Li, "Polymorphous FeS corrosion products of pipeline steel under highly sour conditions," *Corrosion Science* 102, (2016): p. 103-113.
12. E.B. Backensto, R.D. Drew, C.C. Stapleford, "High Temperature Hydrogen Sulfide Corrosion," *Corrosion*, 12, 1 (1956): p. 22-32.
13. A.V. Skalunov, G.V. Sretenskaya, G.A. Tsarkov, "Effect of hydrogen sulfide and temperature on the corrosion behavior of high-alloy metals in precipitation baths for viscose manufacture," *Fibre Chemistry* 18, 4 (1987): p. 321-325.
14. Y. Qi, H. Luo, S. Zheng, C. Chen, Z. Lv, M. Xiong, "Effect of Temperature on the Corrosion Behavior of Carbon Steel in Hydrogen Sulphide Environments," *International Journal of Electrochemical Science* 9, (2014): p. 2101-2112.
15. Y. Zheng, J. Ning, B. Brown, S. Nescic, "Advancement in Predictive Modeling of Mild Steel Corrosion in CO<sub>2</sub>-and H<sub>2</sub>S-Containing Environments," *Corrosion* 72, 5 (2016): p. 679-691.
16. T. Tanupabrungsun, D. Young, B. Brown, S. Nescic, "Construction and Verification of Pourbaix Diagrams for CO<sub>2</sub> Corrosion of Mild Steel Valid up to 250°C," CORROSION/2012, paper no. 0001418 (Salt Lake City, UT: NACE, 2012).
17. R. Thodla, F. Gui, K. Evans, C. Joia, I. P. Baptista, "Corrosion Fatigue Performance of Super 13 CR, Duplex 2205 and 2507 for Riser Applications," CORROSION/2010, paper no. 10312 (San Antonio, TX: NACE, 2010).
18. J. Ning, Y. Zheng, B. Brown, D. Young, S. Nescic, "Construction and Verification of Pourbaix Diagrams for Hydrogen Sulfide Corrosion of Mild Steel," CORROSION/2015, paper no. 5507 (Dallas, TX: NACE, 2015).
19. F.E. Jones, G.L. Harris, "ITS-90 density of water formulation for volumetric standards calibration," *Journal of research of the National Institute of Standards and Technology* 97, (1992): p. 335-340.
20. O.M. Suleimenov, R.E. Krupp, "Solubility of hydrogen sulfide in pure water and in NaCl solutions, from 20 to 320°C and at saturation pressures," *Geochimica et Cosmochimica Acta* 58, 11 (1994): p. 2433-2444.
21. O.M. Suleimenov, T.M. Seward, "A spectrophotometric study of hydrogen sulphide ionisation in aqueous solutions to 350°C," *Geochimica et Cosmochimica Acta* 61, 24 (1997): p. 5187-5198.
22. J. Ning, Y. Zheng, D. Young, B. Brown, S. Nescic, "Thermodynamic Study of Hydrogen Sulfide Corrosion of Mild Steel," *Corrosion* 70, 4 (2014): p. 375-389.

23. D.D.N. Singh, A. Kumar, "A Fresh Look at ASTM G 1-90 Solution Recommended for Cleaning of Corrosion Products Formed on Iron and Steels," *Corrosion* 59, 11 (2003): p. 1029-1036.
24. J. Ning, Y. Zheng, B. Brown, D. Young, S. Nescic, "The Role of Iron Sulfide Polymorphism in Localized H<sub>2</sub>S Corrosion of Mild Steel," *CORROSION/2016*, paper no. 7502 (Vancouver, BC: NACE, 2016).
25. L.G. Benning, R.T. Wilkin, H.L. Barnes, "Reaction pathways in the Fe-S system below 100°C," *Chemical Geology* 167, 1 (2000): p. 25-51.